Journal of Power Sources 255 (2014) 394–403

Contents lists available at ScienceDirect

Journal of Power Sources

journal homepage: www.elsevier.com/locate/jpowsour

Cobalt and molybdenum activated electrodes in foam based alkaline electrolysis cells at 150–250 °C and 40 bar

Frank Allebrod*, Christodoulos Chatzichristodoulou, Mogens B. Mogensen

Technical University of Denmark, Department of Energy Conversion and Storage, Frederiksborgvej 399, P.O. Box 49, 4000 Roskilde, Denmark

HIGHLIGHTS

- A new type of alkaline electrolysis cell has been developed.
- Co- and Mo-oxide electro-catalysts on nickel foam based gas diffusion electrodes were used.
- Potassium hydroxide as electrolyte was immobilized in a porous $SrTiO_3$ structure.
- The performance of the cells have been analyzed at 150–250 °C at 40 bar.
- Current densities of 1.1 A cm^{-2} and 2.3 A cm^{-2} have been measured at 1.5 V and 1.75 V.

ARTICLE INFO

Article history:
Received 27 September 2013
Received in revised form
27 December 2013
Accepted 1 January 2014
Available online 15 January 2014

Keywords:
Alkaline electrolysis
High temperature
High pressure
Gas diffusion electrodes
Metal foam

ABSTRACT

A new type of alkaline electrolysis cells with nickel foam based gas diffusion electrodes and KOH (aq) immobilized in mesoporous $SrTiO_3$ has been developed and tested at temperatures of 150 °C, 200 °C and 250 °C at a pressure of 40 bar. Two cells have been characterized during the 270 h long test, using impedance spectroscopy, cyclic voltammetry and chronoamperometry at an applied cell voltage of 1.5 V, 1.625 V and 1.75 V. The performance of the electrolysis cells was improved by the addition of cobalt oxide and molybdenum oxide as nano sized electro-catalysts. At 250 °C current densities of 1.1 A cm^{-2} and 2.3 A cm^{-2} were obtained at cell voltages of 1.5 V and 1.75 V, respectively.

© 2014 Elsevier B.V. All rights reserved.

1. Introduction

1.1. Alkaline electrolysis

The political decision to change the energy supply system from fossil fuels towards renewable energies in many European countries, specially Denmark and Germany with very ambitious goals, raises the demand for effective, ecologic and economic energy storage systems. Hydrogen produced by renewable energy through water electrolysis can fulfill these demands [1]. Alkaline electrolysis has proven to be reliable and efficient [2], but both production and investment costs need to be reduced, e.g. by pressurized electrolysis in order to reduce compression costs [3]. Higher operational temperatures can improve the electrical efficiency and thereby reduce electricity consumption for a certain current density significantly. This has been described in earlier work [4].

The principle functionality of an alkaline electrolysis cell is well described in literature [5–7] and has also been discussed in Refs. [8,4]. The cell voltage, U_{cell}, at a certain current density, i, depends mainly on the operation temperature [9] and pressure [3], the electrolyte concentration (conductivity) [10], the choice of electro-catalyst and its concentration [11] and the microstructure of the electrodes. Major losses are the cathodic overvoltage, η_{H_2}, the anodic overvoltage, η_{O_2}, and ohmic losses in the electrolyte.

A new electrolysis cell type has been developed and is described. A porous structure in which the liquid electrolyte is immobilized by capillary forces can be used as a combination of diaphragm and electrolyte [4]. The hydrogen evolution reaction (HER) and the oxygen evolution reaction (OER) take place at gas diffusion electrodes (GDEs), similar to those used in high temperature solid oxide fuel cells (SOFC) and solid oxide electrolysis cells (SOEC) [12] with the aim of reducing or eliminating bubble formation. GDEs have to be highly electronic conductive to minimize

* Corresponding author.
E-mail addresses: fkal@dtu.dk, frank-allebrod@gmx.de (F. Allebrod), ccha@dtu.dk (C. Chatzichristodoulou), momo@dtu.dk (M.B. Mogensen).

0378-7753/$ – see front matter © 2014 Elsevier B.V. All rights reserved.
http://dx.doi.org/10.1016/j.jpowsour.2014.01.024

ohmic losses, and porous to allow the produced gases to escape while steam flows into the cell towards the triple phase boundary (TPB). Since the electrochemical reactions take place at the TPB, it is important that the TPB-length is as long as possible [13].

The performance of an alkaline electrolysis cell is typically expressed as the current density as a function of the applied cell voltage. Commercially available alkaline electrolysis systems typically operate at cell voltages at or above 1.75 V with current densities around 0.2 A cm^{-2} [7] at 70–80 °C operation temperature. Divisek et al. reached a current density of 400 mA cm^{-2} at a cell voltage of 1.55 V and a temperature of 100 °C on a Raney-nickel cell [2]. A current density of 1 A cm^{-2} was reported at 2.12 V on a cell with a $NiFe(OH)_2$ anode and a Pt coated steel cathode [14] at 58 °C. A current density of 1 A cm^{-2} has been reported from Wendt et al. at a cell voltage of 1.8 V and 1.65 V for cell temperatures of 120 °C and 156 °C, respectively [15]. Studies of alkaline electrolysis cells with GDEs similar to the ones analyzed in this study, but with Ag deposited as electro-catalyst for the OER or without added electrocatalyst, were analyzed at temperatures up to 250 °C in previous work [4]. A current density of up to 2.0 A cm^{-2} was shown at 1.75 V. System efficiencies of state of the art alkaline electrolysis systems with values between 47 and 82% have been summarized by Ursúa et al. [6]. It should be noted that the current density is an important factor if the system efficiency has to be analyzed since it is easy to operate electrolysis systems at a high efficiency if the current density, and by that the power density (in W cm^{-2} of the electrolysis cell) is low enough. In order for alkaline electrolysis systems to become economically attractive it is important to operate them at high current densities and efficiencies.

1.2. Electro-catalysts for the OER and HER

Electro-catalysts for the OER [16,17] and HER [18,19] have been extensively studied for alkaline electrolysis. Nickel is often used as electrode material since it is stable against corrosion in alkaline media and nickel oxyhydroxide shows good electrochemical performance without further activation [20]. Co_3O_4 and Co-based spinel oxides are known to be among the best electro-catalysts for the OER in alkaline media and are successfully used in combinations with Ni supported electrodes. An in situ activation process, where $Co(NO_3)_2$ was mixed to the electrolyte (KOH) of a traditional, immersed electrolysis cell to form Co_3O_4 by anodic deposition during electrolysis, showed a reduction of the electrode overpotential η_{O_2} by 80–140 mV at 1 A cm^{-2} and a temperature of 120 °C [21, Fig. 3]. Other utilized preparation methods, with catalyst deposition prior to operation (ex situ) are for example thermal decomposition, spray pyrolysis, electrostatic spray deposition, sol–gel, precipitation, electro-spinning, anodic oxidation of alloys, rheological phase reaction and pyrolysis, gel hydrothermal oxidation, and electrodeposition techniques. A review of the named methods to produce Co-oxide coatings has recently been published by Hamdani et al. [22].

Although the anodic overpotential caused by the OER is usually dominating over the cathodic overpotential caused by the HER, it is still relevant to identify corrosion resistant and economically attractive catalysts for the HER. Raney-nickel and molybdenum [23] are preferred electro-catalysts for the HER. A combination of the advantageous properties of Raney Ni and Mo as an alloy electro-catalyst leads to a reduction of η_{H_2} by 360 mV (for a perforated Ni sheet) from −430 mV to −70 mV at a current density of 1 A cm^{-2} and a temperature of 70 °C by applying the vacuum plasma spraying process [24].

Nickel foams are widely used and versatile for many purposes [25] and have already been shown to hold promise as components in GDEs for the oxygen reduction reaction ORR in an alkaline fuel cell [26]. Very recent data of an alkaline electrolysis cell with nickel foam electrodes and $NiCo_2O_4$ electro-catalyst, deposited with a direct combustion preparation procedure, for low temperature applications (120 °C) have been presented at the World Hydrogen Energy Conference 2012 in Toronto from Bouzek et al. [27].

More advanced metal foams have recently been developed from Alantum Europe GmbH [28]. The cells analyzed in this research work are a new type of alkaline electrolysis cells [29]. A similar version has been shown to operate at 250 °C and 42 bar [4]. The foam based alkaline electrochemical cells (FobAEC) are produced from metal foams, $SrTiO_3$ as porous matrix to immobilize the aqueous electrolyte (45 wt % KOH). A cobalt- or molybdenum $SrTiO_3$ mixture as electro-catalyst is used in the here presented work in order to further activate the electrodes and increase the performance of the GDEs.

2. Experimental

2.1. Production of electrolysis cells

Circular foam pieces with a diameter of 10 mm are stamped out of the foam sheets with a thickness of 1.0 mm for the nickel foam, and 1.5 mm for the Inconel foam. One layer of nickel foam is pressed uniaxially at approximately 50 N cm^{-2}. Another layer of unpressed nickel foam is placed on top. Circa 30 mg of a mixture of 50 wt% Cobalt (II) hydroxide (99.9% (metals basis), Alfa Aesar product number 012524) and 50 wt% $SrTiO_3$ was placed on top of the foam. Another layer of 200 mg pure $SrTiO_3$ powder was added before 30 mg of a mixture of 30 wt% Molybdenum (VI) oxide (99.95% (metal basis), Alfa Aesar product number 011837), and 70 wt% $SrTiO_3$ was placed on top. One drop of an appropriate binder (MEK in 33% ethanol) was mixed to 100 mg of the perovskite $SrTiO_3$ powder to obtain better adhesion of the powder particles during processing and sintering. One layer of Inconel foam is placed on top of the powder-sandwich.

The whole structure is pressed for 30 s at 13.0 kN cm^{-2}. The cells have then been sintered in air at 450 °C for 2 h with a heating ramp of 100 K h^{-1} followed by a second sintering step in 9 % H_2/Ar at 1000 °C for 6 h with a heating and cooling ramp of 50 K h^{-1}. The produced cells had a diameter of ca. 10 mm with a total height of 1.75 mm, the cathode, anode, and electrolyte thickness were ca. 300 μm, 150 μm and 1300 μm, respectively. The heights have been measured by SEM on a similar cell and may vary by roughly 100 μm since the foam electrodes may penetrate to a varying extent into the electrolyte structure at different locations.

2.2. Electrochemical measurements

Two similar cells were produced as described above. Electrochemical measurements, i.e. electrochemical impedance spectroscopy (EIS), cyclic voltammetry (CV), and chronoamperometric measurements (CAM) (potentiostatic measurements) have been performed in order to determine the cell characteristics during operation. A *Gamry Reference 3000* potentiostat connected to a 8 channel *ECM 8 Electrochemical Multiplexer* were used to conduct the measurements. Cyclic voltammograms or iV-curves were recorded with a sweep rate of 50 mV s^{-1} starting from open circuit voltage (OCV), increasing the cell voltage to 1.75 V, then returning to OCV. EIS has been performed under a cell polarization of 1.5 V. The area specific resistance ASR [mΩ cm^2] and the serial resistance R_s [mΩ cm^2] of the cells were determined from the polarized impedance measurements without further inductance corrections. The polarization resistance R_p [mΩ cm^2] was calculated by $R_p = ASR - R_s$.

The programmed sequence for EIS and CV measurements was a repeating loop of 3 EIS measurements at OCV, prior to polarized EIS,

followed by a CV. CAM were performed for both cells at temperatures of 200 °C and 250 °C in order to determine the steady state characteristics of the cell at an applied cell voltage of 1.5 V, 1.625 V and 1.75 V. The step time has been varied from 2 min to 100 h; high current densities at the elevated cell voltages made a limited testing time necessary in order to avoid strong degradation at an early stage.

A high temperature and pressure electrochemical test station that enables electrochemical testing in a temperature range of 25–280 °C and a pressure range of 1–100 bar in an autoclave was utilized. The entire system, comprising a sample holder for simultaneous measurements of four cells, has been described in detail elsewhere [30].

2.3. Temperature, gas flow profile and partial pressures during testing

The temperature and gas flow profile used to test the produced cells is shown in Table 1. The electrochemical measurements were started at $t_0 + x$ h, where t_0 indicates the starting point of the measurement and x is the time that passed after t_0. The column "time $t_0 + x1 \rightarrow t_0 + x2$" indicates the time span for which the listed settings are valid. H_2, N_2 and $H_2O_{(g)}$(steam) was supplied to the autoclaves chamber; in fact O_2 was also supplied, but it is completely converted to steam in the catalytic burner with part of the supplied H_2.

In order to avoid evaporation or dilution of the immobilized electrolyte, it is necessary to keep the water vapor partial pressure near the equilibrium value with the electrolyte. The equilibrium water vapor partial pressure over aqueous potassium hydroxide solutions, $p_{W,KOH}$, has been described by Balej [31], who showed that an empirical equation can be used to calculate $p_{W,KOH}$ in a temperature range of 0–300 °C and potassium hydroxide (KOH) concentrations of 0–18 m. For a KOH concentration of 45 wt% and temperatures of 150 °C, 200 °C and 250 °C, $p_{W,KOH}$ has been calculated to be 1.67 bar, 5.98 bar and 16.47 bar, respectively. N_2 and H_2 were supplied in addition to H_2O in order to maintain the system pressure constant at 40 bar.

The partial pressures of H_2 (p_{H_2}), steam (p_{H_2O}) as well as $p_{W,KOH}$ over the entire measurement period are listed in Table 1. The steam partial pressure was kept close to $p_{W,KOH}$ to avoid dilution or drying of the electrolyte. In order to compensate for the steam used for the electrolysis process, p_{H_2O} was adjusted to 17.3 bar at $t_0 + 164$ h and to 18.7 bar at $t_0 + 169$ h by reducing the N_2-flow rate and by that also pN_2 (the system pressure was constant during the entire measurement).

3. Results

3.1. Physical structure of the produced cells

After pressing and sintering, the FobAECs were analyzed under the optical microscope. Pictures of the nickel foam side (anode) and the Inconel foam side (cathode) are shown in Fig. 1. The pore size of the compressed foams was between 50 and 100 μm.

Table 1
Overview of the partial pressures p_{H_2}, p_{H_2O} and $p_{W,KOH}$ in [bar] at the relating temperature. The corresponding measurements are evaluated in the listed sections. The total pressure was held constant at 40 bar by balancing with N_2 gas.

Temp. [°C]	Time $t_0 + x1 \rightarrow t_0 + x2$	Section	p_{H_2}	p_{H_2O}	$p_{W,KOH}$
150	3 → 17.5	3.4	0.16	2.3	1.67
150	17.5 → 27	3.4	0.47	1.1	1.67
150	27 → 61	3.4	0.93	1.2	1.67
200	69 → 131	3.5, 3.7.1, 3.7.1	1.4	5.6	6.0
250	139 → 164.5	3.6, 3.7.2, 3.7.2	4.0	16.0	16.5
250	164.5 → 169	3.7.2	4.0–4.7[a]	17.3	16.5
250	169 → 270	3.7.2, 3.7.3, 3.7.3	4.7	18.7	16.5

[a] Linearly increasing.

3.2. Electrode/electrolyte interface

Scanning electron microscopy (SEM) images of the electrodes and the electrode–electrolyte interface are shown in Fig. 2, with the nickel electrode in the upper row and the Inconel in the lower row. A cross section of the cell in the left column shows the nickel foam (light gray, upper left image) and the Inconel foam (light gray, upper right image) facing the porous $SrTiO_3$ structure (dark gray, from now on called *electrolyte structure*). Nickel foam was employed as anode (oxygen-electrode) and Inconel was employed as cathode (hydrogen-electrode). Both electrodes bonds well with the electrolyte structure, offering a long three phase boundary (TPB), although the nickel electrode penetrates deeper into the electrolyte structure, where the electrolyte and the electrodes have no connection to the gas phase. The cracks in the electrolyte structure are attributed to the polishing step of the SEM sample preparation process.

A significant difference between the Inconel and nickel foam electrode is the tortuosity; while the gases can enter or leave the electrodes rather easily on the Inconel side, the higher tortuosity of the nickel foam may lead to gas diffusion limitations at higher current densities. This is a result of the pressing procedure, where the softer nickel foam is compressed more in the direction perpendicular to the cell plane than the stiffer Inconel foam.

The images in the center of Fig. 2 are top views of the same electrodes. The electrolyte structure faces the top of the cell well distributed over the cell for the nickel electrode (upper image) while the Inconel electrode shows foam only. Furthermore it can be seen that the Inconel foams structure is rougher than the nickel one, thereby offering a higher specific surface.

A detailed picture of the electrode/electrolyte interface is shown in the right column of the same figure. The highly porous $SrTiO_3$ electrolyte nano structure (light gray) with a mean pore size of 63 nm (compare [4, Fig. 6]) faces the electrodes (dark gray). On the lower right picture it can also be seen that some of the molybdenum agglomerates on the rough Inconel surface (similar to snow covered mountain peaks).

3.3. Activated electrolyte structure

3.3.1. Cathode

The $SrTiO_3$ powder facing the Inconel cathode has been mixed with molybdenum oxide powder as described in Section 2.1. In Fig. 3 it can be seen that molybdenum particles (Mo) are well distributed in the electrolyte structure (S) with a particle size between 100 nm and 200 nm. The molybdenum has a tendency to agglomerate on the surface of the Inconel foam (Inc).

3.3.2. Anode

Also the $SrTiO_3$ powder facing the nickel anode has been mixed with cobalt oxide powder as described in Section 2.1. In Fig. 4 it can be seen that the cobalt particles (white) are distributed in the electrolyte structure (dark gray) with a pore size around 50–200 nm. There is no tendency for the Co particles to agglomerate at the nickel surface as it was seen in Fig. 3 for molybdenum on the Inconel foam.

3.4. Cell performance at 150 °C

The impedance values ASR [mΩ cm^2] (=R_s + R_p) and R_s [mΩ cm^2] of the cells obtained from $t_0 + 3$ h until $t_0 + 38$ h at 150 °C are shown in Fig. 5. The serial resistance R_s of the cells at 150 °C and

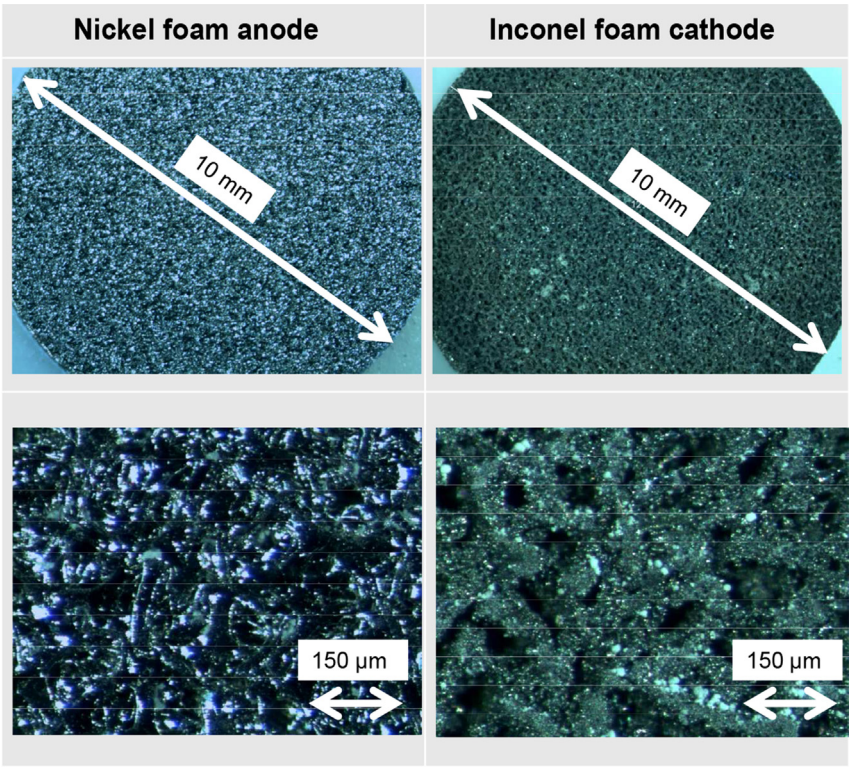

Fig. 1. Optical micro-graphs of the electrodes of a FobAEC showing the nickel anode (left) and Inconel cathode (right). The foam structure is well distributed over the entire electrode without regions that significantly differ from others. Also the porosity seems well distributed over the entire electrode with pore sizes in between 50 µm–100 µm.

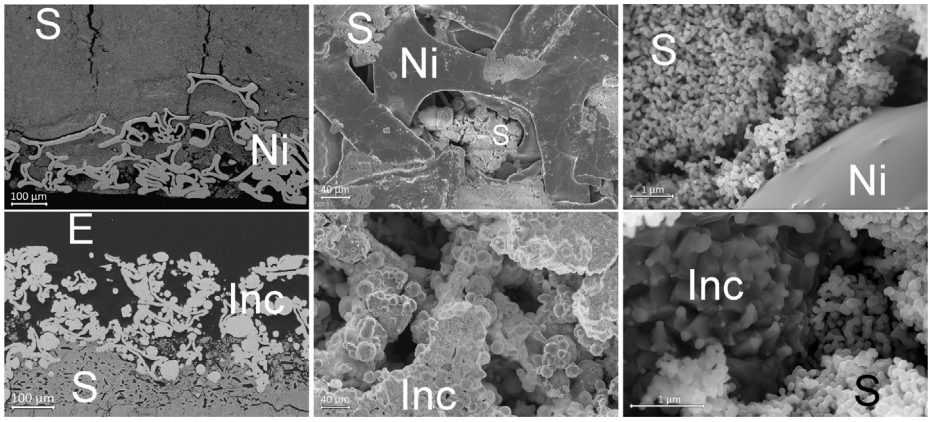

Fig. 2. SEM images of the fabricated cells. Left column: cross-section of the electrodes of a FobAEC showing the nickel foam (Ni) (upper image) and the Inconel foam (lower image) structure in contact with $SrTiO_3$(S) (The dark structure (E) is epoxy used for sample fixation in the microscope). Middle column: top view of the nickel foam anode (upper image) and the Inconel foam cathode (lower image). Lower row: detailed picture of the electrode/electrolyte interface of the nickel foam (upper image) and the Inconel foam (lower image) (before soaking in KOH (aq)).

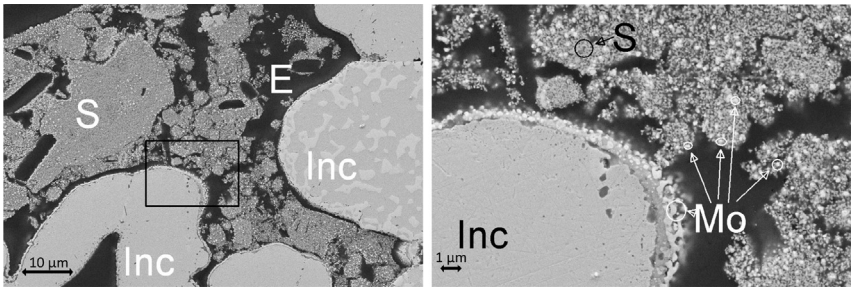

Fig. 3. SEM picture of the cross section of the FobAECs cathode showing the interface between the Inconel foam (Inc) and the $SrTiO_3$ (S) structure containing Mo particles with a size of 100 nm–200 nm and Mo layers distributed along the TPB. E is epoxy for microscopy purposes and not of relevance.

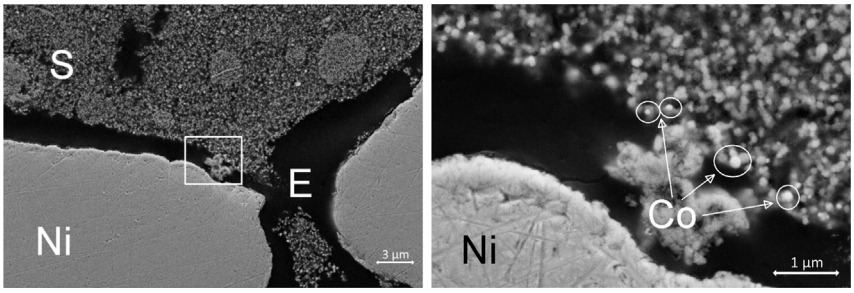

Fig. 4. SEM picture of the interface between the cross section of the FobAECs anode showing the nickel foam (Ni) and the $SrTiO_3$ structure with Co particles distributed along the TPB.

40 bar were initially 220 mΩ cm^2 for both cells. It increased to 244 mΩ cm^2 after a measurement time of 18 h for cell A and to 276 mΩ cm^2 for cell B. The ASR increased from 534 mΩ cm^2 and 431 mΩ cm^2 to 919 mΩ cm^2 and 858 mΩ cm^2 for cell A and B, respectively. The degradation of the cells was faster in the first 10 h than thereafter, they stabilized at $t_0 + 24$ h of measurement time. The R_s stabilized at 237 mΩ cm^2 for cell A and 263 mΩ cm^2 for cell B while the ASR stabilized at 793 mΩ cm^2 for cell A and 815 mΩ cm^2 for cell B until $t_0 + 38$ h. It should be noted that the gas composition was changed at $t_0 + 18$ h towards a more reducing atmosphere and a higher inert gas flow rate (compare Table 1).

Current densities of 725 mA cm^{-2} and 920 mA cm^{-2} at 1.75 V were recorded before stabilization at the beginning of the measurements ($t_0 + 4$ h → $t_0 + 20$ h) for cell A and B, respectively. Fig. 6 shows the iV curves recorded in the period $t_0 + 24$ h → $t_0 + 38$ h. Cell A showed stable current density of 590 mA cm^{-2} at 1.75 V while for cell B it decreased from 690 mA cm^{-2} to 633 mA cm^{-2}. The OCV increased during this time from 800 mV to 885 mV for cell A and from 792 mV to 885 mV for cell B.

3.5. Cell performance at 200 °C

Results from impedance measurements at a constant temperature of 200 °C and a pressure of 40 bar are shown in Fig. 7. The measurement sequence was started at $t_0 + 73$ h and was performed for 12 h. The performance during this period was rather stable, R_s increased slightly from 202 mΩ cm^2 to 212 mΩ cm^2 for cell A and from 179 mΩ cm^2 to 192 mΩ cm^2 for cell B. The ASR of cell A improved from 472 mΩ cm^2 to 454 mΩ cm^2 while it increased from 390 mΩ cm^2 to 418 mΩ cm^2 for cell B.

Fig. 8 shows the iV curves that were recorded during the same period (t_0 + 73 h →t_0 + 85 h) at 200 °C. The obtained current density for cell A decreased slightly from 985 mA cm^{-2} to 960 mA cm^{-2} at 1.75 V while for cell B it decreased from 1069 mA cm^{-2} to 1029 mA cm^{-2}. The OCV increased during this time from 1010 mV to 1045 mV for both cells.

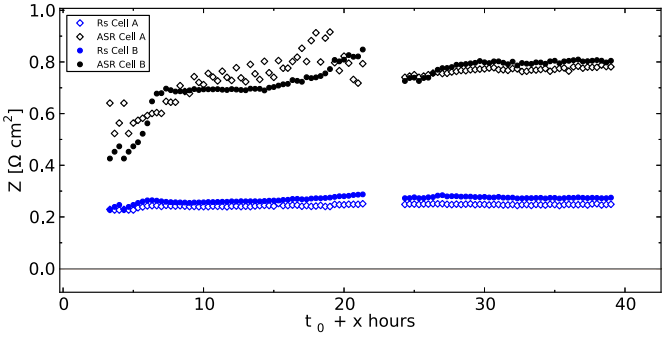

Fig. 5. EIS results showing R_s and ASR (=R_s + R_p) during the first 38 h at 150 °C at a polarization of 1.5 V of cell A (◇) and cell B (○). The measurement interval was 20 min for each cell.

3.6. Cell performance at 250 °C

Impedance measurements at a constant temperature of 250 °C and a pressure of 40 bar were performed after potentiostatic tests at 200 °C executed (shown below in Section 3.7.1). The measurement sequence was started 145 h after the entire measurement started and lasted for 9 h. Results are shown in Fig. 9: R_s decreased initially from 150 mΩ cm^2 to 133 mΩ cm^2, before it increased again to 153 mΩ cm^2 for cell A. For cell B R_s increased from 130 mΩ cm^2 to 191 mΩ cm^2. The ASR for cell A varied between 215 mΩ cm^2 and 234 mΩ cm^2, while it increased from 236 mΩ cm^2 to 327 mΩ cm^2 for cell B.

Fig. 10 shows the current densities recorded at 250 °C at $t_0 + 147$ h, $t_0 + 150$ h and $t_0 + 153$ h. The obtained current density for cell A decreased from a value of 2.29 A cm^{-2} to 2.03 A cm^{-2} at 1.75 V. It can also be seen that a second peak occurred at 520 mV for the iV curve of cell A 147 h after t_0. The peak reduced its current density from 900 mA cm^{-2} to 825 mA cm^{-2} to 518 mA cm^{-2} while the voltage at which the peak appeared decreased from 512 mV to 480 mV to 418 mV for the time of 147 h, 150 h, and 153 h after t_0, respectively. The origin of these peaks and the further peaks up to a cell voltage of 1.0 V may originate from oxidation/reduction of electrode components and will be further analyzed in future measurements. Cell B showed 2.23 A cm^{-2} at the beginning of the sequence with a relatively fast degradation resulting in a reduced current density of 1.51 A cm^{-2} 6 h after the sequence started. The OCV increased from 50 mV to 70 mV for cell A as well as for cell B; the relatively low value for the OCV is addressed in the discussion.

3.7. Potentiostatic tests

3.7.1. Chronoamperometric measurements at 200 °C

Chronoamperometric measurements were performed commonly at a cell polarization of 1.5 V for longer periods (up to 100 h) and at 1.625 V and 1.75 V for shorter times (up to 20 min) to prevent too fast degradation of the cell. Initial tests at 200 °C on cell A and B with applied cell voltages of 1.5 V, 1.625 V and 1.75 V and a step time of 20 min at each cell voltage showed a relatively stable current density of 322 mA cm^{-2}, 582 mA cm^{-2} and 830 mA cm^{-2} for cell A, respectively, and 379 mA cm^{-2}, 625 mA cm^{-2} and 943 mA cm^{-2}, respectively, for cell B. Impedance measurements indicated that R_s increased by ca. 20 mΩ cm^2 to 220 mΩ cm^2 for cell A and to 212 mΩ cm^2 for cell B. ASR increased from 335 mΩ cm^2 to 385 mΩ cm^2 for cell A and from 332 mΩ cm^2 to 351 mΩ cm^2 for cell B. The OCV was recorded for 120 s after the CAM. It decreased within this time from 1.35 V to 1.2 V for cell A and from 1.29 V to

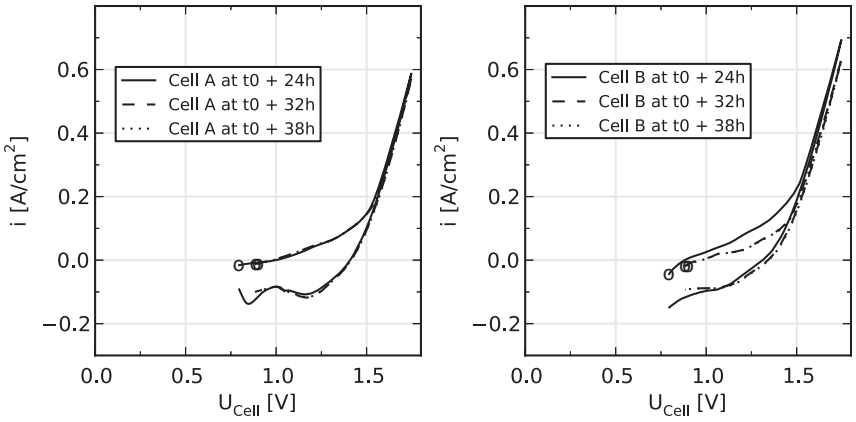

Fig. 6. iV curves of cell A (left) and cell B (right) during 14 h at 150 °C and 40 bar, started at t_0 + 24 h and ending at t_0 + 38 h. The marker (○) indicates the beginning point of the measurement (OCV).

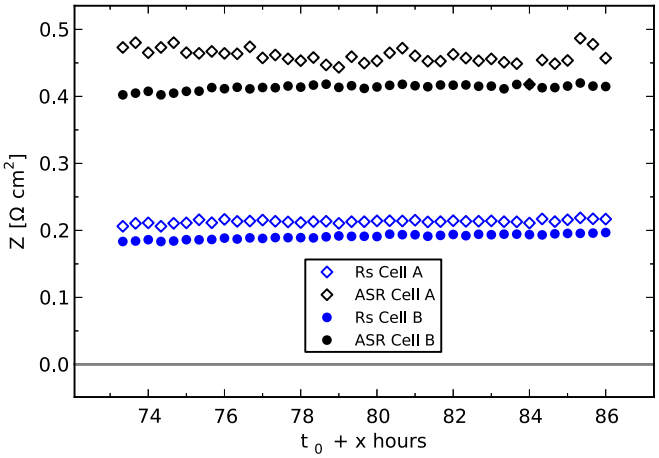

Fig. 7. EIS results showing R_s and ASR started at t_0 + 73 h and ending at t_0 + 85 h at 200 °C at a polarization of 1.5 V of cell A (◇) and cell B (○). The measurement interval was 20 min for each cell.

0.80 V for cell B. It should be pointed out here that there was no continuous flow of O_2 to the anode and reduction of the OCV is natural. The reduction of the OCV will be further analyzed in the discussion.

A following CAM on cell A started at t_0 + 85 h for 24 h at 1.5 V and 20 min at 1.625 V and 1.75 V. The potentiostatic measurement at 1.5 V applied cell voltage, as shown in the upper part of Fig. 11, showed a stable current density of ca. 320 mA cm^{-2}, the current densities at 1.625 V and 1.75 V were 568 mA cm^{-2} and 848 mA cm^{-2}, respectively, at the end of the 20 min lasting steps. R_s increased from 210 mΩ cm^2 to 237 mΩ cm^2, and the ASR from 457 mΩ cm^2 to 512 mΩ cm^2 before and after the measurement as shown in the lower part of Fig. 11.

3.7.2. Chronoamperometric measurements at 250 °C and 40 bar

Further CAM were performed at 250 °C and 40 bar for cell A and cell B for 60 min at 1.5 V. Cell A showed slightly increasing current density from 720 mA cm^{-2} to 814 mA cm^{-2} and cell B showed increasing current density from 950 mA cm^{-2} to 1.05 A cm^{-2}. R_s of cell A improved from 157 mΩ cm^2 to 153 mΩ cm^2, the ASR was found to be constant at 241 mΩ cm^2. R_s of cell B increased from 156 mΩ cm^2 to 162 mΩ cm^2, and the ASR was found to be 227 mΩ cm^2 before and 242 mΩ cm^2 after the measurement.

A 100 h lasting CAM was performed at t_0 + 155 h, at an applied cell voltage of 1.5 V on cell B. Results are presented in the upper part of Fig. 12. The current density was 670 mA cm^{-2} at the beginning of the measurement and decreased rapidly to 520 mA cm^{-2} within 5 h (30 mA cm^{-2} h^{-1}). The current density reduced by 5 mA cm^{-2} h^{-1} to 450 mA cm^{-2} during the following 9.0 h. After 14 h of

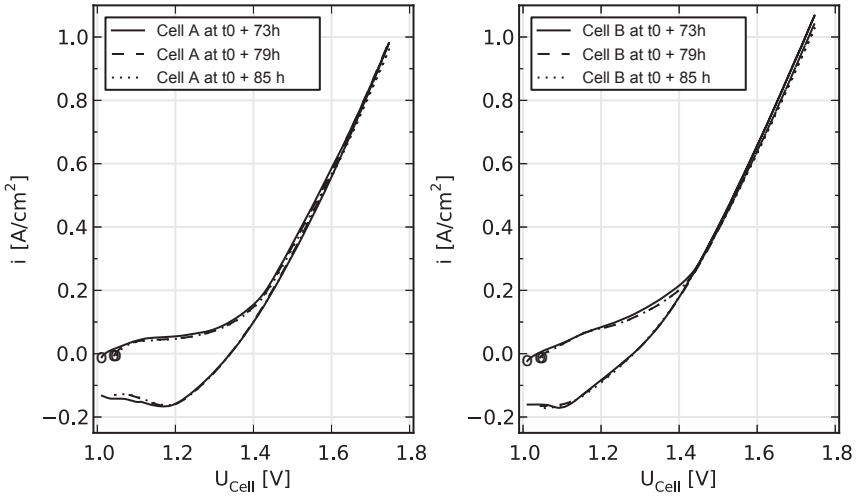

Fig. 8. iV curves of the two tested cells at 200 °C and 40 bar, starting at t_0 + 73 h and ending at t_0 + 85 h. The marker (○) indicates the beginning point of the measurement (OCV).

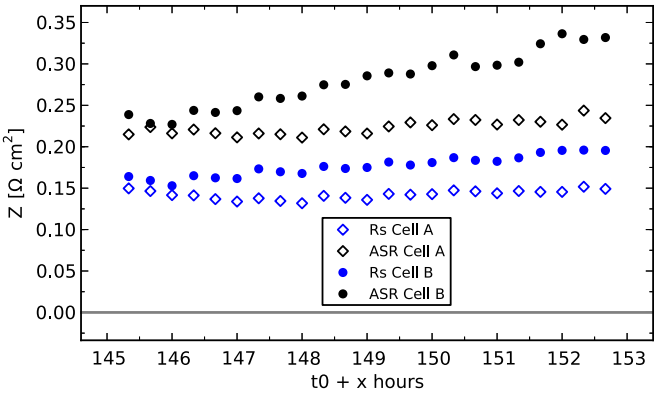

Fig. 9. EIS results showing R_s and ASR starting at $t_0 + 145$ h and ending at $t_0 + 153$ h at 250 °C at a polarization of 1.5 V for cell A (◇) and cell B (○). The measurement interval was 20 min for each cell.

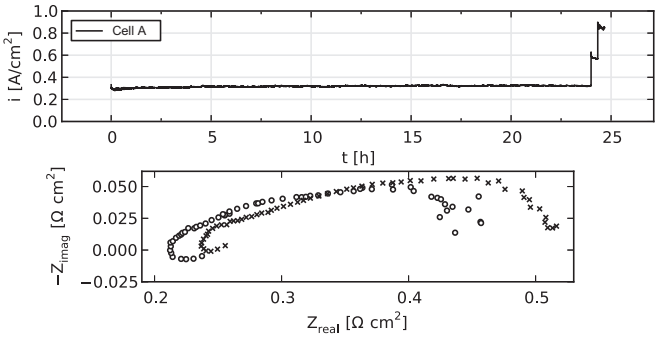

Fig. 11. CAM of cell A at 200 °C and 40 bar showing a step function for the applied cell voltage of 1.5 V, 1.625 V and 1.75 V for a time of 24 h at 1.5 V and a 20 min/step at 1.625 V and 1.75 V started at $t_0 + 85$ h with the corresponding impedance plots at a polarization of 1.5 V before (○) and after (×) the CAM.

measurement time, at $t_0 + 169$ h, the degradation stopped for a period of 6 h after increasing p_{H_2O} to 18.7 bar (compare Table 1), but resumed to degrade with reduced degradation rate (2.2 mA cm^{-2} h^{-1}) to 304 mA cm^{-2} after 100 h. Impedance measurements have been performed before and after the CAM and are shown in Fig. 12 in the Nyquist plane. The R_s increased from 190 mΩ cm^2 to 572 mΩ cm^2, and the ASR was found to be 350 mΩ cm^2 before and 1.2 Ω cm^2 after the measurement, so the R_p increased from 160 mΩ cm^2 to 628 mΩ cm^2.

3.7.3. Chronoamperometric measurement for 1 h at 250 °C and 40 bar

After the 100 h long CAM on cell B, another CAM was started on cell A to examine its performance after this time of being idle. The cell reached its original performance of 1.0 A cm^{-2} after an activation time of about one hour at an applied cell voltage of 1.5 V, as shown in Fig. 13. At 1.625 V it was around 1.60 A cm^{-2} and at 1.75 V it reached a value of 2.30 A cm^{-2}. Impedance measurements performed before and after the CAM are shown in Fig. 13. R_s decreased slightly from 191 mΩ cm^2 to 188 mΩ cm^2, the ASR was found to be 297 mΩ cm^2 before and 268 mΩ cm^2 after the measurement, and the R_p improved from 106 mΩ cm^2 to 80 mΩ cm^2. The OCV recorded directly after the last step of the CAM dropped almost linearly during 120 s from 1.21 V to 0.57 V.

4. Discussion

4.1. Conductivity of the electrolyte

The serial resistance R_s decreased with increasing temperature. In Table 2 it can be seen how R_s and the corresponding conductivity of the cell, σ_{Cell}, developed with temperature, where $R_{s,min}$ is the minimal value, $R_{s,mean}$ the averaged value for the given period and $R_{s,max}$ is the highest measured value at each temperature. It should be noted that only the values from the EIS measurements under steady conditions (data from Figs. 5, 7 and 9) were taken into consideration for the values given in Table 2. The corresponding conductivities are given in the same table in comparison with the conductivity of aqueous KOH in a porous matrix, $\sigma_{Cell,KOH}$, measured in earlier work [10]. Since the empirical equation from Ref. [10] used to calculate $\sigma_{Cell,KOH}$ is valid only up to 200 °C, $\sigma_{Cell,KOH}$ at 250 °C should be treated with caution. The here measured conductivities are in fair accordance with $\sigma_{Cell,KOH}$, indicating that the ohmic resistance of the electrolyte structure is the main contribution to the serial resistance of the cell. Variances can occur from dilution or drying of the electrolyte as well as from contact resistances in the setup, for example due to oxidation of the Ni foam at the oxygen electrode.

4.2. Peak performance of the cells at 150, 200 and 250 °C

Impedance and performance data have been obtained at temperatures of 150 °C, 200 °C and 250 °C. The best values after

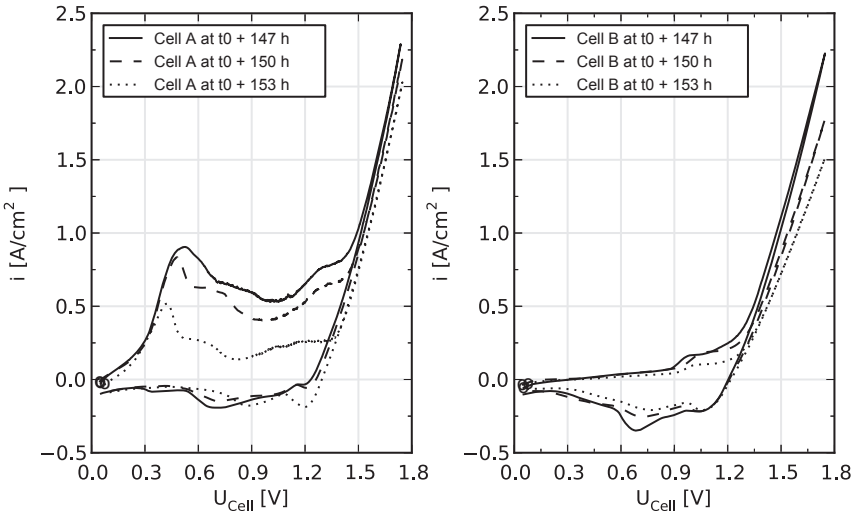

Fig. 10. iV curves of the two tested cells at 250 °C starting at $t_0 + 147$ h and ending at $t_0 + 153$ h. The marker (○) indicates the beginning point of the measurement (OCV).

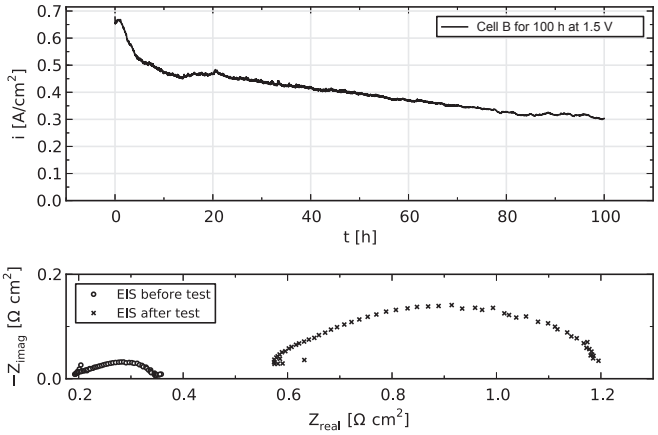

Fig. 12. CAM of Cell B at 250 °C and 40 bar at an applied cell voltage of 1.5 V for 100 h started at t_0 + 155 h (upper figure) with the corresponding impedance plots at a polarization of 1.5 V before (○) and after (×) the CAM.

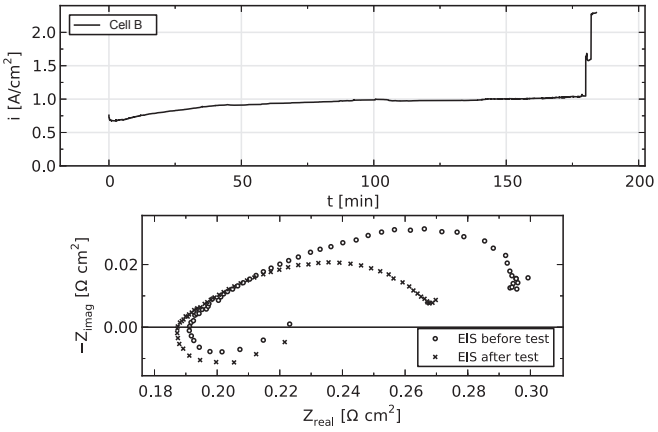

Fig. 13. CAM of Cell A at 250 °C and 40 bar at 1.5 V for 180 min, 1.625 and 1.75 V for of 2 min/step, started at t_0 + 264 h. The corresponding impedance plots at a polarization of 1.5 V before (○) and after (×) the CAM.

stabilization at the specific temperature have been extracted from the results and are shown in Table 2. As discussed before a significant reduction of R_s has been measured with increasing temperature; it reduced by a factor of 1.83 for cell A and by a factor of 1.77 for cell B from 150 °C to 250 °C. This is in good accordance with data from previous work [10]. An even more significant reduction has been obtained for R_p which has been reduced by a factor of 6.45 for cell A and by a factor of 6.00 for cell B from 150 °C to 250 °C. Furthermore, the obtained results show that the current density at a certain cell voltage is more limited by the electrode performance at lower temperatures ($R_s/R_p \approx 0.5$ at 150 °C). It is almost equally limited by the electrolyte conductivity and the electrode polarization resistance at 200 °C ($R_s/R_p \approx 1$), and at 250 °C the electrolyte conductivity becomes the main rate limiting factor ($R_s/R_p \approx 2$). This indicates that further improvement of the cells can be achieved by reduction of R_s, i.e. reduction of the electrolyte thickness.

It is furthermore obvious that the activation with Co and Mo improved the cell performance if compared to results from earlier work, where similar produced cells reached lower, but still remarkably high current densities of 0.68 A cm^{-2} and 1.57 A cm^{-2} at 1.5 V and 1.75 V, respectively, at 240 °C and 39 bar (Inconel foam cathode and Nickel foam cathode without further electrocatalyst). A similar cell with Ag deposited on the Nickel anode and Inconel foam without further electro-catalyst reached 0.9 A cm^{-2} and 2.0 A cm^{-2} at 1.5 V and 1.75 V, respectively, at 247 °C and 42 bar [4].

The power density of a electrochemical cell (P_{cell} [W cm^{-2}]) can be calculated by $P_{cell} = I_{cell}U_{cell}$. The cells presented in this work obtained a power density of up to 4 W cm^{-2} at a cell voltage of 1.75 V, 250 °C and 40 bar. If this is compared to power densities of commercially available systems operated at 1.75 V and 0.2 A cm^{-2} with 0.35 W cm^{-2}, it is obvious that the cell stack area of an electrolysis system with the here presented cells can be reduced by an order of magnitude for the same power and thereby lead to significantly reduced investment costs, although the design of such a system will be a challenging task.

4.3. Development of the OCV

The OCV measured before CV measurements at 150 °C from t_0 + 24 h to t_0 + 38 h (compare Fig. 6) showed an increasing OCV from ca. 800 to 880 mV. A comparable behavior was shown for the OCV measured before CV measurements at 200 °C from t_0 + 73 h to t_0 + 85 h (compare Fig. 8), where the OCV increased from 1.01 V to 1.05 V. A surprisingly low OCV was measured at 250 °C (compare Fig. 10) from t_0 + 123 h to t_0 + 129 h with a value between 50 mV and 70 mV only.

A possible explanation lies in the gas composition in the autoclave, shown in Table 1. The p_{H_2} was relatively low at temperatures of 150 °C with 0.16 bar from t_0 + 3 h to t_0 + 17.5 h, 0.47 bar from t_0 + 17.5 h to t_0 + 27 h and 0.93 bar from t_0 + 27 h to t_0 + 60 h. At a temperature of 200 °C it was set to 1.4 bar from t_0 + 67 h to t_0 + 131 h whereas p_{H_2} was between 4.0 bar and 4.7 bar from t_0 + 135 h to t_0 + 270 h. The higher p_{H_2} most likely led to a faster diffusion of the hydrogen gas from the autoclaves atmosphere to the cells anode when the cell is not polarized, thereby reducing the OCV. A faster diffusion path for H_2 can occur through the cell if the electrolyte has partially dried out forming an open channel through which gas can diffuse directly from the cathode to the anode (diffusion path A, with a corresponding time constant $\tau \sim 2$ s). This could for example happen if the feed of steam to the electrodes is too low due to inaccuracies in the mass flow controllers or incomplete reaction of the H_2/O_2 mixture in the catalytic burner. OCV measurements after polarization indicated that gas diffusion occurred at a rate corresponding to 100–200 mV min^{-1} decrease in OCV. This decrease rate is too slow to be attributed to gas diffusion through open channels in the electrolyte. The decrease in OCV is therefore associated with diffusion through the liquid electrolyte (diffusion path B, $\tau \sim 1000$ s) and diffusion from the autoclaves compartment to the anode of the cell (diffusion path C, $\tau \sim 100$ s). It

Table 2
Comparison of the minimal ($R_{S,min}$), averaged ($R_{S,mean}$) and highest ($R_{S,max}$) measured serial resistance during steady state periods along with the corresponding conductivities $\sigma_{Cell,max}$, $\sigma_{Cell,mean}$ and $\sigma_{Cell,min}$ and a reference value obtained from previous work [10]. Data from Figs. 5, 7 and 9 were taken into account.

Temp.[°C]	Time span t_0 + (start–end [h])	$R_{S,min}$ [mΩ cm^2] Cell A/B	$R_{S,mean}$ [mΩ cm^2] Cell A/B	$R_{S,max}$ [mΩ cm^2] Cell A/B	$\sigma_{Cell,max}$ [S cm^{-1}] Cell A/B	$\sigma_{Cell,mean}$ [S cm^{-1}] Cell A/B	$\sigma_{Cell,min}$ [S cm^{-1}] Cell A/B	$\sigma_{Cell,KOH}$ [S cm^{-1}] [10]
150	3–22	220/221	234/252	244/276	0.75/0.75	0.71/0.66	0.68/0.60	0.59
200	73–86	201/179	210/187	214/192	0.82/0.93	0.79/0.89	0.77/0.86	0.84
250	145–153	131/130	143/171	153/191	1.26/1.27	1.16/0.97	1.08/0.87	(1.18)

can therefore be concluded that the reduction of OCV arose primarily due to gas diffusion from the autoclave compartment to the anode. The time constants were estimated from the relation $\tau = x^2/2D$, using the value of $x = 2$, 2, 30 mm for the diffusion lengths for diffusion path A, B, and C, respectively, and the corresponding diffusion coefficients D.

4.4. Chronoamperometric measurements

CAM were performed at 200 °C and 250 °C. Most measurements showed an initial decrease in current density for a short time after applying a specific voltage. It can partly be explained by the fact that the system is not in steady state directly after incrementing the voltage, i.e. the gas composition at the electrodes changes during electrolysis. The obtained current density at 200 °C is in good accordance with the value obtained by CV. The maximum measured current density with CV at 1.5 V was 310 mA cm^{-2}, while the CAM showed 322 mA cm^{-2} at the same applied cell voltage of 1.5 V. Apart from the initial passivation observed during the first 1–10 min after applying a specific cell voltage, no further passivation or degradation occurred during the 24 h lasting test at 1.5 V. Nevertheless, R_s and R_p were increased by 27 mΩ cm^2 and 55 mΩ cm^2, respectively. This is probably associated with the higher current densities recorded while applying higher cell voltages at the end of the CAM (the constant cell voltage for the CAM was increased in two equal steps from 1.5 V to 1.75 V).

The CAM performed at 250 °C showed also stable or even activating performance at a cell voltage of 1.5 V, although the performance has not been as good as measured by CV for cell A for which 814 mA cm^{-2} was obtained by CAM and 1.05 A cm^{-2} by CV. A possible explanation is the fact that the cell is measured in a steady state condition during the potentiostatic measurements, which is not the case for CV at 50 mV s^{-1}. Nevertheless, cell B was in very good accordance with 1.05 A cm^{-2} obtained by CAM and 1.11 A cm^{-2} by CV.

Although the cells showed limited degradation during the CV measurements, as shown in Fig. 10, an extended CAM for cell B was initiated for a time of 100 h at 1.5 V and 250 °C (compare Fig. 12). Both R_s and R_p increased strongly during the 100 h long CAM. SEM analysis of a similar cell used in a 350 h test under galvanostatic conditions indicates that too fast oxidation of the anodic nickel foam based electrode and the current collector could be the cause for the decreased performance. Further details can be found elsewhere [8].

Cell A was left unbiased during the 100 h test of cell B, before another CAM was performed. The cell performance improved significantly during this time. A possible explanation relates to condensation of steam and subsequent flooding of the anode or cathode during the passive time, which gradually evaporates again during operation. In a following CAM of the same cell (cell A) for 3 h, further activation took place until the initial performance of 1.05 A cm^{-2} at 1.5 V applied cell voltage was recovered (compare Fig. 13). Impedance measurements after this measurement confirmed that the cell did not suffer from strong degradation since R_s was 188 mΩ cm^2 and with that only 37 mΩ cm^2 higher than the best measured value for that cell. Even more complete recovery was obtained for R_p, which was 80 mΩ cm^2 and with that only 3 mΩ cm^2 higher than the best measured value shown in Table 3.

4.5. Differences in the analyzed cells

The cells were prepared similar and were sintered at the same time in one batch. Differences in their electrochemical performance during the measurements have been recorded. They may occur from small differences in the cell structure, for example uneven distribution of the powders before pressing, or differences of the foams topography. Furthermore they may result from a different stage of degradation of the electrodes or measurement system interface. Furthermore, the performance critically depends on accurate control of the operating conditions, especially cell temperature and p_{H_2O}; a too high p_{H_2O} may dilute the immobilized KOH during operation while a too low p_{H_2O} ($<p_{W,KOH}$) will result in partial evaporation of water and subsequent concentration of the electrolyte. Both would lead to a higher R_s at 250 °C since the selected electrolyte concentration (45 wt% KOH) yields the optimum conductivity at this temperature.

5. Conclusion

Two similar electrolysis cells with metal foam based electrodes (Mo activated Inconel foam cathode, Co activated Ni foam anode) and aqueous KOH electrolyte immobilized in a mesoporous matrix of $SrTiO_3$ were tested at 150 °C, 200 °C and 250 °C and a pressure of 40 bar. The performance of the cells increased with increasing temperature. The conductivity of the immobilized electrolyte (45 wt% KOH) at 150 °C, 200 °C and 250 °C was at least 0.75 S cm^{-1}, 0.93 S cm^{-1} and 1.27 S cm^{-1}, respectively, as deduced from the serial resistance of the cells. At an applied cell voltage of 1.5 V current densities of 0.23 A cm^{-2}, 0.36 A cm^{-2} and 1.11 A cm^{-2} were obtained at 150 °C, 200 °C and 250 °C, respectively. The current densities obtained at an applied cell voltage of 1.75 V were as high as 0.69 A cm^{-2}, 0.9 A cm^{-2} and 2.3 A cm^{-2} at 150 °C, 200 °C and 250 °C, respectively. An initial passivation, which stabilized after 24 h was observed for both cells at the beginning of the investigation at 150 °C. The measurements at 200 °C showed stable values, among others a 24 h potentiostatic measurement at 1.5 V showed a constant current density of ca. 320 mA cm^{-2}. Activation and passivation processes were observed at 250 °C; i.e. one cell degraded strongly during a 100 h lasting test, while the other recovered its initial performance during this time, thereby indicating that at least one of the indicated passivation processes is reversible. Possible degradation mechanisms could be oxidation of the anodic current collector or the anode itself, concentration changes in the electrolyte resulting in flooding or drying of the electrodes, or bubble formation in the electrodes that were not hydrophobic. Since commercially available alkaline electrolysis systems operate at current densities of about 0.2 A cm^{-2} at 1.75 V it is obvious that the here proposed cell concept can increase the power density by an order of magnitude, thereby reducing the material and investment costs significantly. This requires the

Table 3
Peak performance data of the measured cells at temperatures of 150 °C, 200 °C and 250 °C.

Temp. [°C]	Time t_0 + [h] (Cell A/B)	R_S [mΩ cm^2] Cell A/B	ASR [mΩ cm^2] Cell A/B	R_p [mΩ cm^2] Cell A/B	I_{Cell} [A cm^{-2}] at U_{Cell} = 1.5 V Cell A/B	I_{Cell} [A cm^{-2}] at U_{Cell} = 1.75 V Cell A/B
150	24/24	240/268	737/730	497/462	0.14/0.23	0.59/0.69
200	112/117	202/186	450/400	248/214	0.31/0.36	1.00/1.1
250	150/148	131/151	208/228	77/77	1.05/1.11	2.3/2.23

design of an electrolyzer feasible to operate at high temperature and pressure which remains a challenging task for future research and development. Implementing the principal possibility of reversible operation in fuel cell mode of the here proposed cells, which remains to be demonstrated, opens the possibility to store and recover electrical energy as needed.

Acknowledgments

The financial support from the 2nd Generation Alkaline Electrolysis Project, EUDP 63011-0200, is gratefully acknowledged. The authors are also thankful for additional financial support from the "Catalysis for Sustainable Energy initiative", funded by the Danish Ministry of Science, Technology and Innovation. Furthermore we are thankful for the supply of metal foams by Alantum Germany GmbH.

References

[1] Ø. Ulleberg, T. Nakken, A. Eté, Int. J. Hydrogen Energy 35 (5) (2010) 1841–1852.
[2] J. Divisek, P. Malinowski, J. Mergel, H. Schmitz, Int. J. Hydrogen Energy 13 (3) (1988) 141–150.
[3] K. Onda, T. Kyakuno, K. Hattori, K. Ito, J. Power Sources 132 (1–2) (2004) 64–70.
[4] Frank Allebrod, Christodoulos Chatzichristodoulou, Mogens B. Mogensen, J. Power Sources 229 (2013) 22–31.
[5] Detlef Stolten, Alkaline Electrolysis – Introduction and Overview, in: Hydrogen and Fuel Cells: Fundamentals, Technologies and Applications, Wiley-VCH, 2010, p. 245.
[6] A. Ursúa, L.M. Gandís, P. Sanchis, Proc. IEEE 100 (2) (2012) 410–426.
[7] Kai Zeng, Dongke Zhang, Prog. Energy Combust. Sci. 36 (3) (2010) 307–326.
[8] Frank Allebrod, High Temperature and Pressure Alkaline Electrolysis, PhD thesis, DTU, Department of Energy Conversion and Storage, 2013.
[9] Ø. Ulleberg, Int. J. Hydrogen Energy 28 (1) (2003) 21–33.
[10] Frank Allebrod, Christodoulos Chatzichristodoulou, Pia Lolk Mollerup, Mogens B. Mogensen, Int. J. Hydrogen Energy 37 (21) (2012) 16505–16514.
[11] Derek Pletcher, Xiaohong Li, Int. J. Hydrogen Energy 36 (23) (2011) 15089–15104.
[12] Ruth Knibbe, Anne Hauch, Johan Hjelm, Sune D. Ebbesen, Mogens Mogensen, Green 16 (2011) 141–169.
[13] P.S. Jørgensen, K.V. Hansen, R. Larsen, J.R. Bowen, J. Power Sources 195 (24) (12/15 2010) 8168–8176.
[14] X. Li, F.C. Walsh, D. Pletcher, Phys. Chem. Chem. Phys. 13 (3) (2011) 1162–1167.
[15] H. Wendt, H. Hofmann, Int. J. Hydrogen Energy 10 (6) (1985) 375–381.
[16] J. Balej, Int. J. Hydrogen Energy 10 (2) (1985) 89–99.
[17] S. Trasatti, Electrochim. Acta 29 (11) (11 1984) 1503–1512.
[18] J.K. Nørskov, T. Bligaard, A. Logadottir, J.R. Kitchin, J.G. Chen, S. Pandelov, U. Stimming, J. Electrochem. Soc. 152 (3) (2005) J23–J26.
[19] L.A. Kibler, Chem. Phys. Chem. 7 (5) (2006) 985–991.
[20] Y. Zhang, X. Cao, H. Yuan, W. Zhang, Z. Zhou, Int. J. Hydrogen Energy 24 (6) (1999) 529–536.
[21] T. Schmidt, H. Wendt, Electrochim. Acta 39 (11–12) (1994) 1763–1767.
[22] M. Hamdani, R.N. Singh, P. Chartier, Int. J. Electrochem. Sci. 5 (4) (2010) 556–577.
[23] J. Divisek, H. Schmitz, J. Balej, J. Appl. Electrochem. 19 (4) (1989) 519–530.
[24] G. Schiller, R. Henne, V. Borck, J. Therm. Spray Technol. 4 (2) (1995) 185–194.
[25] John Banhart, Prog. Mater. Sci. 46 (6) (2001) 559–632.
[26] F. Bidault, D.J.L. Brett, P.H. Middleton, N. Abson, N.P. Brandon, Int. J. Hydrogen Energy 34 (16) (2009) 6799–6808.
[27] K. Bouzek, J. Hnát, M. Paidar, J. Schauer, J. Žitka, in: World Hydrogen Energy Congress 2012, Toronto, 2012.
[28] M. Gerber, R. Poss, A. Tillmann, G. Walther, B. Kieback, K. Wolf, F. Hanel, J. Sandwich Struct. Mater. 14 (2) (2012) 181–196.
[29] F. Allebrod, C. Chatzichristodoulou, P.L. Mollerup, M.B. Mogensen, High Performance Reversible Electrochemical Cell for H_2O Electrolysis or Conversion of CO_2 and H_2O to Fuel, Patent Pending No. 12164019.7-2119, 2012.
[30] C. Chatzichristodoulou, F. Allebrod, M. Mogensen, Rev. Sci. Instrum. 84 (5) (2013) 054101–054101–12.
[31] J. Balej, Int. J. Hydrogen Energy 10 (4) (1985) 233–243.